

# Singlet-Oxygen-Sensitizing Near-Infrared-Fluorescent Multimodal Nanoparticles

Edakkattuparambil Sidharth Shibu, Sakiko Sugino, Kenji Ono, Hironobu Saito, Ayama Nishioka, Shohei Yamamura, Makoto Sawada, Yoshio Nosaka, and Vasudevanpillai Biju\*

Photoresponsive multimodal nanomaterials have become prevalent in biomedical imaging and nanomedicine settings owing to their unique optical properties, flexible surface chemistry, and ability to accommodate multiple functions.<sup>[1]</sup> The basis of multimodality is co-registration of anatomical structures or physiological conditions by combining modalities among positron emission tomography (PET),<sup>[2]</sup> X-ray computed tomography (CT),<sup>[3]</sup> ultrasonography,<sup>[4]</sup> magnetic resonance imaging (MRI),<sup>[2]</sup> and fluorescent molecular tomography (FMT).<sup>[5]</sup> Although X-ray-based images provide high spatial resolution, radiation damage and related health risks are topics of public concerns. Thus, safer imaging modalities such as MRI and near-infrared fluorescence molecular tomography (NIR-FMT) have become popular.<sup>[6]</sup> Also, combined MRI and fluorescence contrast agents receive considerable attention in applications such as disease diagnosis,<sup>[7]</sup> gene/drug delivery,<sup>[8]</sup> and phototherapy.<sup>[9a]</sup> Such contrast agents are fabricated by recruiting of organic dyes,<sup>[8b]</sup> semiconductor quantum dots (QDs),<sup>[7a]</sup> upconversion nanoparticles,<sup>[9a]</sup> or rare-earth complexes<sup>[9b]</sup> to the surface of magnetic nanomaterials or vice versa. Although, organic dyes are abundant in various colors and reactive forms, their potentials for bioimaging is limited because of the poor photostability, narrow absorption and broad emission bands, toxicity, and sensitivity to local environment.<sup>[10]</sup> Despite the bright, stable, and size-dependent tunable photoluminescence (PL) of chalcogenide QDs,<sup>[11]</sup> their major limitation is toxicity.<sup>[5]</sup> Thus, nontoxic and NIR-fluorescent nanomaterials are greatly investigated.

Upconversion nanoparticles,<sup>[9a]</sup> lanthanide complexes,<sup>[9b]</sup> and noble-metal quantum clusters (QCs)<sup>[12]</sup> are emerging nontoxic fluorescent materials. QCs in this context refer to

those with only a few atoms in the core and exhibit NIR fluorescence because of “molecule-like” electronic transitions. Apart from the nontoxic nature, the large Stokes shift and NIR fluorescence of these materials help us for not only trimming down the background fluorescence but also obtaining deeper penetration into biological specimens. Among different NIR fluorophores mentioned above, gold QCs have become relevant in bioimaging owing to their simple synthesis, nontoxic nature, and high photostability.<sup>[12,13]</sup> Chemical reduction of gold ions followed by stabilization of gold atoms with simple ligands or large proteins<sup>[13]</sup> are standard for the synthesis of gold QCs. Besides the inherent fluorescence of QCs or other nanomaterials, an additional fluorescence modality can be stimulated by the photosensitization of oxygen.<sup>[14]</sup> Nevertheless, the generation of singlet oxygen (<sup>1</sup>O<sub>2</sub>) from NIR-emitting nanoparticles and in situ bioimaging using the enhanced fluorescence from the singlet oxygen sensor dyes is yet to be evaluated, which can be a promising method for multimodal bioimaging and photodynamic therapy (PDT).

Multimodal nanoparticles (MNPs) in this work are fabricated by the conjugation of biotinylated NIR-fluorescent gold QCs to streptavidin-functionalized Fe<sub>3</sub>O<sub>4</sub> NPs, which is followed by <sup>1</sup>O<sub>2</sub>-sensitized photouncaging of the fluorescence of fluorescein in the methylnanthracene-fluorescein-caged conjugate. The photostability of QCs over organic dyes allows us to detect them even at single-molecule level. MNPs are successively converted into bioimaging probes by the conjugation of the epidermal growth factor (EGF), which is known for their EGF receptor-mediated extracellular labeling and endocytosis. The efficient intracellular delivery of MNPs allows us to combine NIR fluorescence and MRI for live cell imaging. Yet another interesting property of QCs is the long-living excited state (> 500 ns),<sup>[15]</sup> which is sufficient to sensitize dissolved oxygen and produce <sup>1</sup>O<sub>2</sub>. Photosensitized production of <sup>1</sup>O<sub>2</sub> is monitored in the NIR window (1270 nm) or using a singlet oxygen sensor green (SOSG) dye, which uncages into green-fluorescent endoperoxide upon reaction with <sup>1</sup>O<sub>2</sub> in solutions or human lung epithelial adenocarcinoma cells (H1650). Apart from the NIR fluorescence and MRI contrasts offered by the probes, the green fluorescence of the endoperoxide of SOSG triggered by <sup>1</sup>O<sub>2</sub> provides us with a third modality for live cell imaging.

Figure 1A summarizes different steps involved in the synthesis of QCs and MNPs. The synthesized QC is biotinylated using biotin NHS ester or conjugated with a photouncaging ligand, and anchored to streptavidin-functionalized

[\*] Dr. E. S. Shibu, Dr. S. Sugino, Dr. S. Yamamura, Prof. Dr. V. Biju  
Health Research Institute  
National Institute of Advanced Industrial Science and  
Technology (AIST), Takamatsu, Kagawa 761-0395 (Japan)  
and  
PRESTO (Japan) Science and Technology Agency (JST) (Japan)  
E-mail: v.biju@aist.go.jp  
A. Nishioka  
Kagawa University, Takamatsu, Kagawa 761-0396 (Japan)  
H. Saito, Prof. Y. Nosaka  
Department of Materials Science and  
Technology Nagaoka Technological University Nagaoka (Japan)  
Prof. K. Ono, Prof. M. Sawada  
Research Institute of Environmental Medicine Nagoya University  
Nagoya 464-8601 (Japan)

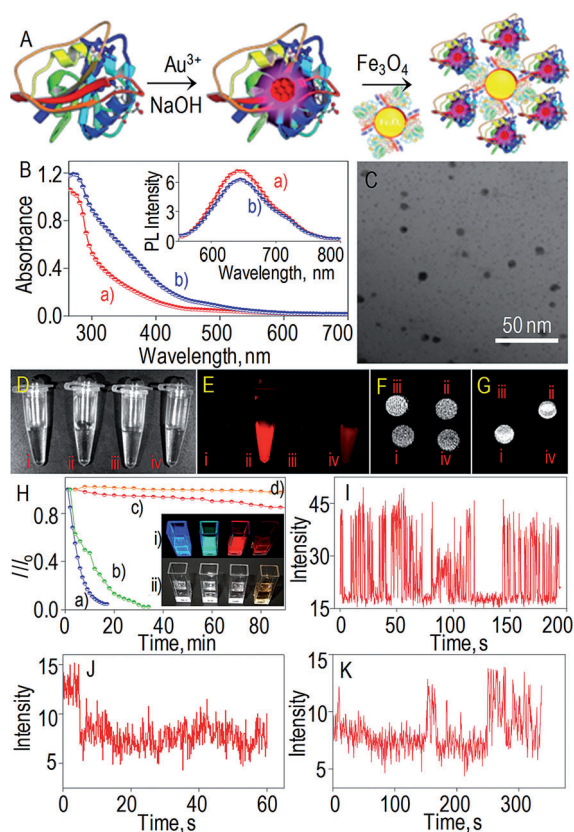


**Figure 1.** A) Synthesis of QCs and MNPs. B) UV/Vis absorption and PL spectra (inset) of a) QCs and b) MNPs. C) TEM image of MNPs. D) Bright-field, E) fluorescence, and F)  $T_1$ - and G)  $T_2$ -weighted MRI of a solution of i) PBS, ii) QCs, iii)  $\text{Fe}_3\text{O}_4$  NPs, and iv) MNPs. H) Plot of  $I/I_0$  versus illumination time for a) coumarin, b) Hoechst, c) QC, and d) QD. Inset: photographs of the same solutions taken under i) UV lamp and ii) day light. I–K) Single-molecule PL intensity trajectories of I) QD and QC J) in air and K) in  $\text{N}_2$  atmosphere.

$\text{Fe}_3\text{O}_4$  NPs. TEM images of isolated MNPs are shown in Figure 1 C. Absorbance of a QC in the 300–450 nm window (Figure 1 B) is attributed to the interband ( $sp \leftarrow d$ ) and intraband ( $sp \leftarrow sp$ ) transitions; whereas the absorbance beyond 450 nm is due to a HOMO–LUMO transition within the QCs.<sup>[12b]</sup> The PL spectrum of the QCs (inset of Figure 1 B) shows an intense NIR emission irrespective of the excitation wavelength. The broad absorption band of the QCs allows us to activate NIR fluorescence by choosing any visible excitation wavelength. UV/Vis absorption and PL spectra of MNPs resemble the integrated features of both QCs and  $\text{Fe}_3\text{O}_4$  NPs. To further confirm the bimodality of MNPs, fluorescence images and  $T_1$ - and  $T_2$ -weighted MRI of the samples are recorded (Figure 1 E–G). Here, the difference in the MRI contrasts is the choice of two scanning parameters, namely the repetition time ( $T_R$ ) and echo delay time ( $T_E$ ). In  $T_2$ -weighted MRI, long  $T_R$  and  $T_E$  give dark contrast to magnetizing materials.

The photostability of fluorescence contrast agents is an important parameter for bioimaging. To evaluate the photostability of QCs and MNPs, we have recorded and compared the time-dependent PL spectra of QCs with those of CdSe/

ZnS QDs and organic dyes at 405 nm excitation. A plot of  $I/I_0$  versus the illumination time (Figure 1 H) shows high photostability of the QCs, which is comparable to the photostability of QDs. We also evaluate the photostability of the QCs at single-molecule level. Under ambient conditions, the PL intensity trajectory of single QCs show fast photobleaching in single steps (Figure 1 J), which suggests photo-oxidation. Photostability of QCs could be extended over several minutes in  $\text{N}_2$  atmosphere (Figure 1 K), which allows us to observe stochastic fluctuations in the PL intensity of QCs, a behavior similar to the blinking of QDs (Figure 1 I).

We investigate the origin of single-molecule photobleaching by recording and analyzing the photosensitized  $^1\text{O}_2$  production by QCs. Although the  $^1\text{O}_2$  production by organic molecules or QDs is widely known,<sup>[16]</sup> activation of  $^1\text{O}_2$  by QCs is a quite new phenomenon. The general mechanism underlying the photosensitized production of  $^1\text{O}_2$  involves energy transfer from the long-living excited state of a photosensitizer to oxygen ( $^3\text{O}_2$ ). Subsequent radiative relaxation of  $^1\text{O}_2$  causes NIR luminescence of about 1270 nm. The lifetime of QCs shows fast (ns) and slow ( $\mu\text{s}$ ) components, which are attributed to prompt emission and thermally activated delayed emission.<sup>[15]</sup> Efficient delayed emission in QCs suggests the probability to photosensitize  $^3\text{O}_2$  and produce  $^1\text{O}_2$ , which is investigated by recording and analyzing the PL decay profiles of QCs under both  $\text{O}_2$  and  $\text{N}_2$  atmospheres (Figure 2 A). Interestingly, the PL lifetime of QCs in air (ca. 365 ns) gradually increases up to 640 ns under  $\text{N}_2$  purging. Conversely, the PL lifetime of QCs recorded under  $\text{N}_2$  atmosphere decreases as the sample is purged with air. In other words, the long-living excited state of QCs under  $\text{N}_2$  atmosphere and the short lifetime in the presence of oxygen

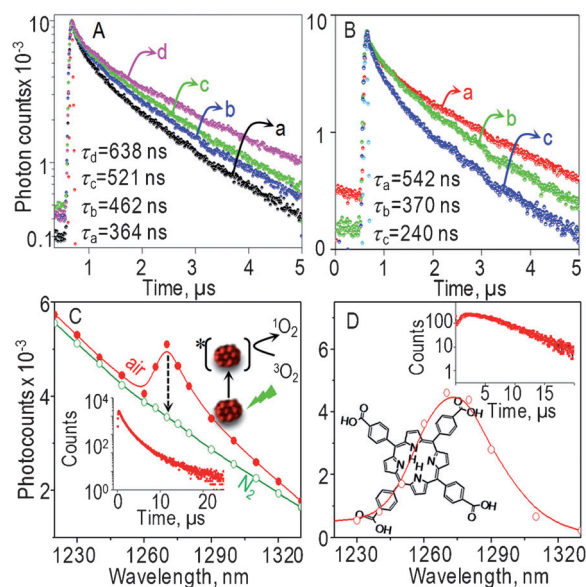


**Figure 2.** A) PL decay profiles of QCs under a) saturation by air and b–d) purging by  $\text{N}_2$  for b) 30, c) 45, and d) 120 minutes. B) Power-dependent PL decay profiles of QCs under a) 0.6, b) 6, and c)  $60 \text{ W cm}^{-2}$  at 532 nm excitation. C, D) Luminescence spectra of  $^1\text{O}_2$  generated by C) QCs and D) TCPP. Insets: PL decay profiles of  $^1\text{O}_2$  produced by QCs and TCPP.

suggest that the production of  $^1\text{O}_2$  by QCs follows the general mechanism of photosensitization. Furthermore, considerable decrease of the PL lifetime (from 542 to 240 ns) or increased production of  $^1\text{O}_2$  is observed as the excitation power intensity is increased from about 0.6 to 60  $\text{W cm}^{-2}$  (Figure 2B).

NIR luminescence band at about 1270 nm with a decay constant of about  $2 \times 10^{-5}$  s in  $\text{D}_2\text{O}$  is the characteristic feature of  $^1\text{O}_2$ ,<sup>[17]</sup> which is clearly visible for air-saturated aqueous solutions of QCs and MNPs excited at 532 nm (Figure 2C). We also compare the NIR luminescence spectrum of  $^1\text{O}_2$  produced by QCs with that by the standard {*meso*-tetra (4-carboxyphenyl)} porphyrin, (TCPP, Figure 2D). Resemblance of the luminescence band at about 1270 nm for QC/MNP and TCPP samples supports QC-based production of  $^1\text{O}_2$ . Although  $^1\text{O}_2$  is produced by photosensitization, molecules such as  $\text{N}_2$  and  $\text{NaN}_3$  efficiently quench  $^1\text{O}_2$ .<sup>[17]</sup> Thus, to further confirm the production of  $^1\text{O}_2$ , we have purged  $\text{N}_2$  gas through QCs or MNPs dissolved in  $\text{D}_2\text{O}$ . Interestingly, the characteristic luminescence of  $^1\text{O}_2$  at about 1270 nm disappears from  $\text{N}_2$ -saturated solutions. Next, we employ SOSG for monitoring of the photosensitization process. SOSG is a conjugate between fluorescein and methylantracene, where the fluorescence of fluorescein is quenched because of intramolecular electron transfer. It becomes bright-green fluorescent in the presence of  $^1\text{O}_2$  because of the formation of an endoperoxide of methylantracene, in which the intramolecular electron transfer is blocked (Figure 3A). To evaluate the production of  $^1\text{O}_2$  using SOSG, an aqueous solution of QCs is photoactivated at 532 nm in the presence of SOSG. This photoactivation results in the continuous and enormous enhancement of green fluorescence (Figure 3B). On the other hand, fluorescence enhancement is negligible for an equivalent sample kept under dark (Figure 3C). The kinetics of  $^1\text{O}_2$  production as a function of the green fluorescence is given in the inset of Figure 3C. Photosensitized production of  $^1\text{O}_2$  is further evaluated using an array of microchannels supplemented with a mixture of QCs and SOSG. A small sample volume (ca. 2 channel diameter) is illuminated with 532 nm laser (ca. 10  $\text{W cm}^{-2}$ ). After photoactivation for two minutes, many channels are simultaneously observed under 463 nm (for SOSG) illumination (1  $\text{mW cm}^{-2}$ ). Interestingly, the bright green fluorescence of the endoperoxide of SOSG detected only in channels illuminated with 532 nm laser light suggests photosensitized production of  $^1\text{O}_2$  by QCs (Figure 3E).

The green fluorescence of the endoperoxide of SOSG is an additional modality offered by  $^1\text{O}_2$  for bioimaging, which is evaluated using live cells. Lung adenocarcinoma of up to 60% confluency are incubated first with a 10 nM solution of QC-EGF conjugate in Dulbecco's modified eagle medium (DMEM) for 1 h and then with 5 nM solution of SOSG for 10 minutes. After the treatment, the cells are washed and supplemented with DMEM and 10% fetal bovine serum (FBS). Photoactivation of the QCs using 532 nm laser light followed by observation under 400 nm illumination shows bright green intracellular fluorescence (Figure 3G). On the other hand, cells treated with QCs and SOSG, but without photoactivation at 532 nm show only weak fluorescence (Figure 3F), which is because of oxidative stress as a result

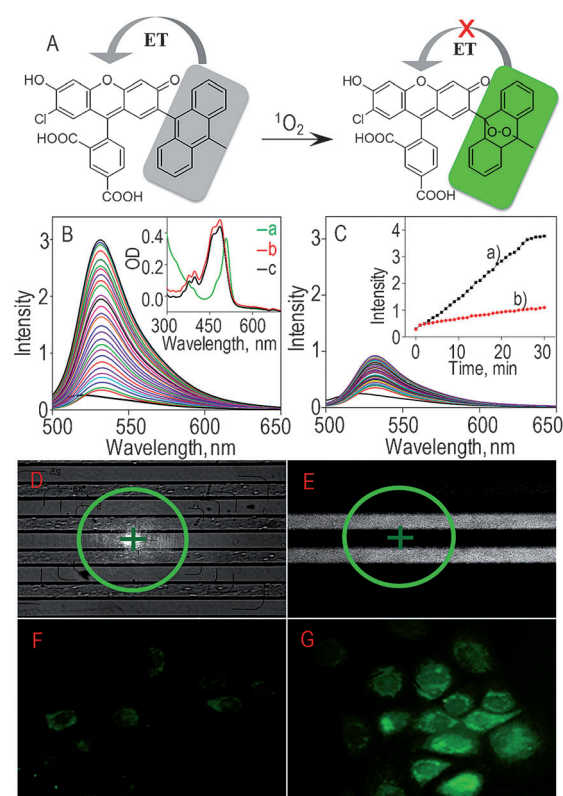


**Figure 3.** A) The structure of SOSG and its reaction with  $^1\text{O}_2$  (ET = electron transfer). B,C) Time-dependent fluorescence spectra of a mixture of SOSG and QCs B) at 532 nm excitation and C) in the dark. Insets: Ba–c) Absorption spectra of SOSG solution after Ba) 0, Bb) 1, and Bc) 30 minutes of photoactivation, and Ca,b) plots of fluorescence intensity versus time under Ca) irradiation at 532 nm and Cb) in the dark. D,E) Images of microchannels filled with SOSG and QCs: D) bright-field image showing the area at 532 nm illumination and E) fluorescence image recorded under wild-field illumination. F,G) Fluorescence images of H1650 cells treated with a mixture of SOSG and QCs: F) without photoactivation of the QCs and G) after five minutes of photoactivation at 532 nm

of imbalance between reactive oxygen species (ROS) formed in cells and the inability of biological systems to detoxify ROS.<sup>[18]</sup> Although antioxidant defense systems such as catalase (CAT), superoxide dismutase (SOD), and glutathione peroxidase (GPx) regulate the homeostasis of ROS, detectable amounts of  $^1\text{O}_2$  will be present in cells. On the other hand, the strong green fluorescence in the cytoplasm of cells treated with QCs suggests a high level of  $^1\text{O}_2$  production by photoactivated QCs, which adds new dimensions such as bioimaging and PDT to QCs.

Apart from the  $^1\text{O}_2$  production ability of QCs, their NIR fluorescence is an important parameter for bioimaging,<sup>[19]</sup> for which poor intracellular delivery efficiency is the major challenge. Here, we show that QCs and MNPs can be efficiently delivered in living cells using EGF and used for combined NIR fluorescence imaging and MRI of cells. H1650 cells are first incubated with 5 nM solution of MNP-EGF or QD-EGF conjugates for 1 h. Successively, the cells are treated with a 5 nM nucleus staining dye syto21, washed with phosphate-buffered saline (PBS) and supplemented with

DMEM and 10% FBS. Intracellular delivery of MNPs or QDs in H1650 cells is investigated using fluorescence microscopy (Figure 4A). Both MNP-EGF and QD-EGF conjugates are transported into the cytoplasm as seen in

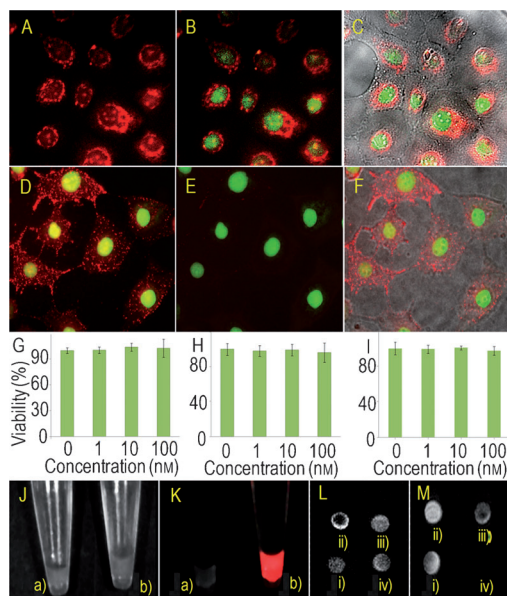


**Figure 4.** Fluorescence and overlaid images of H1650 cells treated with A–C) MNP-EGF conjugates (red) and syto 21 (green), and D–F) QD-EGF conjugates (red) and syto 21 (green). G–I) MTT assay histograms for G)  $\text{Fe}_3\text{O}_4$ , H) QCs, and I) MNPs. J) Bright-field image and K) fluorescence image of a) cell pellets without and b) with labeling using MNPs. L)  $T_1$ - and M)  $T_2$ -weighted MRI of i) PBS, ii) QCs, and iii, iv) cells labeled iii) without and iv) with MNPs.

Figure 4A–F. EGF-mediated endocytosis of MNPs or QDs follows the standard pathway of binding to the extracellular domain of the G-protein-coupled EGF receptor followed by clathrin-mediated endocytosis. Thus, MNPs and QDs are mostly trapped in the *endo*-lysosomal compartments as seen in Figure 4A,D. To ensure the nontoxic nature of QCs,  $\text{Fe}_3\text{O}_4$  NPs and MNPs, we evaluated the mitochondrial reductase enzyme activity of labeled cells by MTT cytotoxicity assay. Over 90% viability (Figure 4G–I) for cells treated with a range of concentration of the labeling agents suggests the non-cytotoxic nature of the nanoparticles involved in this study.

Intracellular delivery of MNPs using EGF allows us to obtain not only NIR fluorescence of QCs and  $^1\text{O}_2$ -sensitized green fluorescence of SOSG but also MRI contrast from labeled cells. For multimodal imaging, labeled cells are washed with PBS, harvested using trypsin, washed, and collected as pellets. Figure 4J,K shows the bright-field and fluorescence images of H1650 cell pellets without and with MNP treatment. Fluorescence images of individual cells (Figure 4A) and cell pellets (Figure 4K) confirm the fluorescence modality provided by MNPs. Figure 4L,M shows  $T_1$ - and  $T_2$ -weighted MRI of cell pellets. The enhanced MRI contrast from cells treated with MNP suggests the potentials of MNPs for multimodal bioimaging.  $T_2$ -weighted MRI

collected from cells treated with MNP helps us to distinguish those from untreated cells because of the enormous dark contrast enhanced under the long echo time. Among different magnetic nanomaterials known so far,  $\text{Fe}_3\text{O}_4$  and Gd-based nanoparticles are common contrast agents in clinical MRI. Thus, the newly developed MNPs composed of  $\text{Fe}_3\text{O}_4$  NPs and nontoxic, NIR-fluorescent and  $^1\text{O}_2$ -sensitizing QCs would be potential multicontrast agents for *in vivo* bioimaging.

In summary, we demonstrate the fabrication of novel photosensitizing, NIR-fluorescent, and magnetic multimodal bioimaging probes and evaluate their intracellular delivery through G-protein-coupled receptors by combined NIR fluorescence imaging and MRI. Exceptionally high photostability of gold QCs in the probes allows us to not only detect them at single-molecule level and in living cells but also incessantly produce  $^1\text{O}_2$ . Photosensitized production of  $^1\text{O}_2$  is monitored in solutions or in human lung epithelial adenocarcinoma cells using a sensor dye that produces green fluorescent endoperoxide of the methylnanthracene-fluorescein-caged conjugate upon reaction with  $^1\text{O}_2$ . In addition to the NIR fluorescence and MRI contrasts offered by the probe, the green fluorescence of the endoperoxide triggered by  $^1\text{O}_2$  provides us with a third modality for live cell imaging. From the best of our knowledge, this is the very first report about QC-based nanoprobe with NIR fluorescence, MRI contrast, and  $^1\text{O}_2$ -sensitized intracellular fluorescence modalities for bioimaging.

## Experimental Section

Instrumentation of fluorescence imaging,<sup>[20a]</sup> PL lifetime studies,<sup>[20b]</sup> and  $^1\text{O}_2$  measurements<sup>[20c]</sup> are provided elsewhere. MRI data are acquired using a small animal imaging equipment (MR Technology, Inc.). Fluorescence images of samples and cell pellets are recorded using a Maestro small animal imaging system (PerkinElmer).

Synthesis of QCs: QCs are synthesized by the controlled reduction of  $\text{Au}^{3+}$  ions in the presence of bovine serum albumin (BSA).<sup>[13c]</sup> Briefly, 1 mL of  $\text{HAuCl}_4$  (5 mM) is added to 1 mL of 300  $\mu\text{M}$  BSA solution under vigorous stirring at 37°C. The pH value of this solution is adjusted by adding 100  $\mu\text{L}$  of 1M NaOH solution with continuous stirring at 37°C for 6 h. During this period, the color of the solution is gradually changed from bright yellow to brown, which is accompanied by intense NIR photoluminescence.

Preparation of the MNP-EGF conjugate: A 1 mM aqueous solution of biotin NHS ester was added to an aqueous solution of QCs (100  $\mu\text{M}$ ). This was followed by stirring the mixture at 25°C for 1 h. During this step, amino groups in BSA are biotinylated, which is purified by dialysis against a membrane for 2 kDa followed by gel filtration on a sephadex G-25 column. In parallel, EGF-biotin is conjugated with streptavidin-functionalized  $\text{Fe}_3\text{O}_4$  NPs in 1:1 ratio. Finally, MNPs are prepared by the conjugation of biotinylated QCs with EGF- $\text{Fe}_3\text{O}_4$  NPs. Similarly, QD-EGF conjugates are prepared by the conjugation of streptavidin-functionalized QDs with biotinylated EGF at 1:1 ratio.

Received: May 17, 2013

Revised: July 14, 2013

Published online: August 13, 2013

**Keywords:** fluorescence · nanomaterials · photochemistry · quantum clusters · singlet oxygen

- [1] a) J. Kim, Y. Piao, T. Hyeon, *Chem. Soc. Rev.* **2009**, *38*, 372; b) L. Frullano, C. Catana, T. Benner, A. D. Sherry, P. Caravan, *Angew. Chem.* **2010**, *122*, 2432–2434; *Angew. Chem. Int. Ed.* **2010**, *49*, 2382–2384; c) L. Röglin, E. H. M. Lempens, E. W. Meijer, *Angew. Chem.* **2011**, *123*, 106–117; *Angew. Chem. Int. Ed.* **2011**, *50*, 102–112; d) L. Cheng, K. Yang, Y. Li, J. Chen, C. Wang, M. Shao, S. T. Lee, Z. Liu, *Angew. Chem.* **2011**, *123*, 7523–7528; *Angew. Chem. Int. Ed.* **2011**, *50*, 7385–7390; e) F. Lux, A. Mignot, P. Mowat, C. Louis, S. Dufort, C. Bernhard, F. Denat, F. Boschetti, C. Brunet, R. Antoine, P. Dugourd, S. Laurent, L. Vander Elst, R. Müller, L. Sancey, V. Josserand, J.-L. Coll, V. Stupar, E. Barbier, C. Rémy, A. Broisat, C. Ghezzi, G. Le Duc, S. Roux, P. Perriat, O. Tillement, *Angew. Chem.* **2011**, *123*, 12507–12511; *Angew. Chem. Int. Ed.* **2011**, *50*, 12299–12303.
- [2] J.-S. Choi, J. C. Park, H. Nah, S. Woo, J. Oh, K. M. Kim, G. J. Cheon, Y. Chang, J. Yoo, J. Cheon, *Angew. Chem.* **2008**, *120*, 6355–6358; *Angew. Chem. Int. Ed.* **2008**, *47*, 6259–6262.
- [3] C. Alric, J. Taleb, G. L. Duc, C. Mandon, C. Billotey, A. L. Meur-Herland, T. Brochard, F. Vocanson, M. Janier, P. Perriat, S. Roux, O. Tillement, *J. Am. Chem. Soc.* **2008**, *130*, 5908–5915.
- [4] M. A. Malvindi, A. Greco, F. Conversano, A. Figuerola, M. Corti, M. Bonora, A. Lascialfari, H. A. Doumari, M. Moscardini, R. Cingolani, G. Gigli, S. Casciaro, T. Pellegrino, A. Ragusa, *Adv. Funct. Mater.* **2011**, *21*, 2548–2555.
- [5] F. Chen, S. Zhang, W. Bu, X. Liu, Y. Chen, Q. He, M. Zhu, L. Zhang, L. Zhou, W. Peng, J. Shi, *Chem. Eur. J.* **2010**, *16*, 11254–11260.
- [6] J. H. Lee, B. Schneider, E. K. Jordan, W. Liu, J. A. Frank, *Adv. Mater.* **2008**, *20*, 2512–2516.
- [7] a) E.-Q. Song, J. Hu, C.-Y. Wen, Z.-Q. Tian, X. Yu, Z.-L. Zhang, Y.-B. Shi, D.-W. Pang, *ACS Nano* **2011**, *5*, 761–770; b) C. Tu, R. Nagao, A. Y. Louie, *Angew. Chem.* **2009**, *121*, 6669–6673; *Angew. Chem. Int. Ed.* **2009**, *48*, 6547–6551.
- [8] a) J. H. Lee, K. Lee, S. H. Moon, Y. Lee, T. G. Park, J. Cheon, *Angew. Chem.* **2009**, *121*, 4238–4243; *Angew. Chem. Int. Ed.* **2009**, *48*, 4174–4179; b) T.-J. Yoon, J.-S. Kim, B. G. Kim, K. N. Yu, M.-H. Cho, J.-K. Lee, *Angew. Chem.* **2005**, *117*, 1092–1095; *Angew. Chem. Int. Ed.* **2005**, *44*, 1068–1071.
- [9] a) F. Chen, S. Zhang, W. Bu, Y. Chen, Q. Xiao, J. Liu, H. Xing, L. Zhou, W. Peng, J. Shi, *Chem. Eur. J.* **2012**, *18*, 7082–7090; b) B. Wang, J. Hai, Q. Wang, T. Li, Z. Yang, *Angew. Chem.* **2011**, *123*, 3119–3122; *Angew. Chem. Int. Ed.* **2011**, *50*, 3063–3066.
- [10] U. Resch-Genger, M. Grabolle, S. C. Jaricot, R. Nitschke, T. Nann, *Nat. Methods* **2008**, *5*, 763–775.
- [11] a) C. B. Murray, D. J. Norris, M. G. Bawendi, *J. Am. Chem. Soc.* **1993**, *115*, 8706–8715; b) V. Biju, T. Itoh, A. Anas, A. Sujith, M. Ishikawa, *Anal. Bioanal. Chem.* **2008**, *391*, 2469–2495; c) I. L. Medintz, H. T. Uyeda, E. R. Goldman, H. Mattoussi, *Nat. Mater.* **2005**, *4*, 435–446; d) V. Biju, T. Itoh, M. Ishikawa, *Chem. Soc. Rev.* **2010**, *39*, 3031–3056; e) V. Biju, Y. Makita, A. Sonoda, H. Yokoyama, Y. Baba, M. Ishikawa, *J. Phys. Chem. B* **2005**, *109*, 13899–13905.
- [12] a) A. C. Templeton, W. P. Wuelfing, R. W. Murray, *Acc. Chem. Res.* **2000**, *33*, 27–36; b) M. Zhu, C. M. Aikens, F. J. Hollander, G. C. Schatz, R. Jin, *J. Am. Chem. Soc.* **2008**, *130*, 5883–5885.
- [13] a) Y. Negishi, Y. Takasugi, S. Sato, H. Yao, K. Kimura, T. Tsukuda, *J. Am. Chem. Soc.* **2004**, *126*, 6518–6519; b) E. S. Shibu, M. A. H. Muhammed, T. Tsukuda, T. Pradeep, *J. Phys. Chem. C* **2008**, *112*, 12168–12176; c) J. Xie, Y. Zheng, J. Y. Ying, *J. Am. Chem. Soc.* **2009**, *131*, 888–889.
- [14] H. Guo, H. Q. Idris, N. M. Idris, Y. Zhang, *Nanomed. Nanotechnol. Biol. Med.* **2010**, *6*, 486–495.
- [15] X. Wen, P. Yu, Y.-R. Toh, A.-C. Hsu, Y.-C. Lee, J. Tang, *J. Phys. Chem. C* **2012**, *116*, 19032–19038.
- [16] A. C. S. Samia, X. Chen, C. Burda, *J. Am. Chem. Soc.* **2003**, *125*, 15736–15737.
- [17] P. R. Ogilby, *Chem. Soc. Rev.* **2010**, *39*, 3181–3209.
- [18] T. Finkel, N. J. Holbrook, *Nature* **2000**, *408*, 239–247.
- [19] L. Polavarapu, M. Manna, Q.-H. Xu, *Nanoscale* **2011**, *3*, 429–434.
- [20] a) N. Kawashima, K. Nakayama, K. Itoh, T. Itoh, M. Ishikawa, V. Biju, *Chem. Eur. J.* **2010**, *16*, 1186–1192; b) V. Biju, A. Anas, H. Akita, E. S. Shibu, T. Itoh, H. Harashima, M. Ishikawa, *ACS Nano* **2012**, *6*, 3776–3788; c) H. Saito, Y. Nosaka, *Chem. Lett.* **2012**, *41*, 1591–1593.